



HAL
open science

Combining photoinduced linkage isomerism and nonlinear optical properties in ruthenium nitrosyl complexes

Artem Mikhailov, Vedran Vuković, Christian Kijatkin, Emmanuel Wenger, Mirco Imlau, Theo Woike, Gennadiy A Kostin, Dominik Schaniel

► **To cite this version:**

Artem Mikhailov, Vedran Vuković, Christian Kijatkin, Emmanuel Wenger, Mirco Imlau, et al.. Combining photoinduced linkage isomerism and nonlinear optical properties in ruthenium nitrosyl complexes. *Acta Crystallographica Section B: Structural Science, Crystal Engineering and Materials* [2014-..], 2019, 75 (6), pp.1152-1163. 10.1107/S205252061901357X . hal-02386531

HAL Id: hal-02386531

<https://hal.univ-lorraine.fr/hal-02386531>

Submitted on 29 Nov 2019

HAL is a multi-disciplinary open access archive for the deposit and dissemination of scientific research documents, whether they are published or not. The documents may come from teaching and research institutions in France or abroad, or from public or private research centers.

L'archive ouverte pluridisciplinaire **HAL**, est destinée au dépôt et à la diffusion de documents scientifiques de niveau recherche, publiés ou non, émanant des établissements d'enseignement et de recherche français ou étrangers, des laboratoires publics ou privés.



Combining photoinduced linkage isomerism and nonlinear optical properties in ruthenium nitrosyl complexes

Artem Mikhailov, Vedran Vuković, Christian Kijatkin, Emmanuel Wenger, Mirco Imlau, Theo Woike, Gennadiy Kostin and Dominik Schaniel

Acta Cryst. (2019). B75, 1152–1163



IUCr Journals

CRYSTALLOGRAPHY JOURNALS ONLINE

Copyright © International Union of Crystallography

Author(s) of this article may load this reprint on their own web site or institutional repository provided that this cover page is retained. Republication of this article or its storage in electronic databases other than as specified above is not permitted without prior permission in writing from the IUCr.

For further information see <http://journals.iucr.org/services/authorrights.html>

Combining photoinduced linkage isomerism and nonlinear optical properties in ruthenium nitrosyl complexes

Artem Mikhailov,^{a,b*} Vedran Vuković,^c Christian Kijatkin,^{d,e} Emmanuel Wenger,^c Mirco Imlau,^d Theo Woike,^c Gennadiy Kostin^{a,b} and Dominik Schaniel^{c*}

Received 11 July 2019

Accepted 4 October 2019

Edited by M. Dusek, Academy of Sciences of the Czech Republic, Czech Republic

Keywords: ruthenium nitrosyl; excited states; linkage isomers; nonlinear optical properties; photocrystallography.

CCDC reference: 1910521

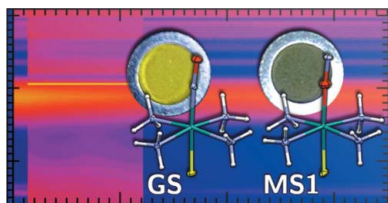
Supporting information: this article has supporting information at journals.iucr.org/b

^aNikolaev Institute of Inorganic Chemistry, Siberian Branch of the Russian Academy of Sciences, 3 Acad. Lavrentiev Avenue, Novosibirsk 630090, Russian Federation, ^bNovosibirsk State University, 1 Pirogova Street, Novosibirsk 630090, Russian Federation, ^cUniversité de Lorraine, CNRS, CRM2, UMR 7036, Nancy 54000, France, ^dDepartment of Physics, Osnabrück University, BarbarasträÙe 7, Osnabrück 49076, Germany, and ^eCenter for Cellular Nanoanalytics, Osnabrück University, BarbarasträÙe 11, Osnabrück 49076, Germany. *Correspondence e-mail: amikhailov@niic.nsc.ru, dominik.schaniel@univ-lorraine.fr

The complex *trans*-[RuNO(NH₃)₄F]SiF₆ was synthesized in quantitative yield and the structure was characterized by X-ray diffraction and spectroscopic methods. The complex crystallizes in the non-centrosymmetric space group *Pn*. Hirshfeld surface analysis revealed that the dominant intermolecular interactions are of types H...F and F...O, which are likely to be responsible for the packing of the molecules in a non-centrosymmetric structure. Irradiation with blue light leads to the formation of Ru–ON (metastable state MS1) and Ru– η^2 -(NO) (metastable state MS2) bond isomers, as shown by IR and UV–Vis spectroscopy. The structural features of the MS1 isomer were elucidated by photocrystallography. The complex exhibits exceptionally good thermal stability of the metastable state MS1, such that it can be populated by light at 290–300 K, which is important for potential applications. The second harmonic (SH) emission can be generated by femtosecond-pulsed irradiation of the complex. The generated SH is rather efficient and stable under long-term exposure. Finally, since both metastable states and harmonic generation can be generated at room temperature, an attempt to drive the SH response by photoisomerization of the nitrosyl ligand was made and is discussed.

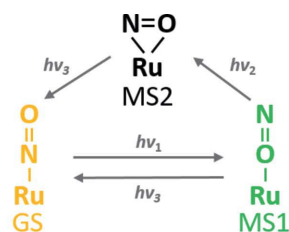
1. Introduction

Molecular materials based on a ruthenium metal centre exhibit a wide range of interesting optical properties. On the one hand, the absorption properties and refractive index of ruthenium nitrosyl complexes can be modified by the photo-generation of metastable states (Schaniel, Cormary *et al.*, 2007; Schaniel, Imlau *et al.*, 2007). These metastable states correspond to different types of coordination of the nitrosyl ligand to the Ru atom, *i.e.* nitrosyl linkage isomers (Coppens *et al.*, 2002). In the ground state (GS) the nitrosyl ligand is coordinated through the N atom (Ru–NO), in metastable state 1 (MS1) through the O atom (Ru–ON) and in metastable state 2 (MS2) the coordination is of side-bond type [Ru– η^2 -(NO)]. An important feature is the possibility to switch reversibly between these three states with light, *i.e.* by using specific photon energies one can drive GS to MS1 ($h\nu_1$) and MS1 to MS2 ($h\nu_2$), while MS1 and MS2 can be transferred back to GS



© 2019 International Union of Crystallography

with a photon energy $h\nu_3$ (see Scheme 1 which shows photo-switching between linkage isomers in ruthenium nitrosyl).



Scheme 1

On the other hand, ruthenium complexes exhibiting nonlinear optical (NLO) properties have been reported, allowing for *e.g.* second-harmonic (SH) generation (Asselberghs *et al.*, 2004). In terms of even-order harmonic generation, the second-order polarizability β [and equivalently the second-order susceptibility $\chi^{(2)}$ for solids] must be non-vanishing, which requires a non-centrosymmetric structure for solid bulk media (Clays & Persoons, 1991; Roke & Gonella, 2012). Third-harmonic (TH) generation, by contrast, is present in any space group and medium. Therefore, the ratio of the emission intensities of SH and TH can be exploited to gauge the NLO properties of new materials with respect to a standard (Kijatkin *et al.*, 2017). Furthermore, a strong molecular dipole moment enhances the polarization effect and leads to even higher SH and TH intensities.

A tailored material for efficient harmonic generation may open up prospective applications, particularly in fields where significant emission signals are required, *e.g.* nonlinear imaging. Based on this, the design of potential molecular materials exhibiting NLO properties comes down to the creation of donor–acceptor interactions between the molecules within the material. Subsequently, a change in the donor–acceptor interaction by reduction of the acceptor or by oxidation of the donor may lead to a change in the NLO response with respect to the conversion efficiency. Redox switching can be triggered by chemical means, electrochemistry or light (Sakaguchi *et al.*, 1989; Coe *et al.*, 1999; Powell *et al.*, 2003). Another interesting idea to control the NLO response was proposed in the work of Akl *et al.* (2013). Based on DFT calculations, those authors showed that the photoswitching of GS to MS1 in ruthenium nitrosyl complexes can induce a significant change in the hyperpolarizability parameter β and might therefore be useful for NLO applications based on the second harmonic, such as for bioimaging (Urban *et al.*, 2012; Su *et al.*, 2017). However, there are certain experimental conditions to be satisfied in order to show that NLO properties can be controlled by photoswitching of nitrosyl linkage isomers. First, the complex needs to be crystallized in a non-centrosymmetric structure in order to produce SH generation in the solid state in the GS. Second, a sufficient amount of MS1 with a reasonable lifetime (ideally at room temperature) is needed in order to measure the change in NLO response upon generation of MS1.

In previous work we have shown that $[\text{RuNO}(\text{py})_4\text{F}](\text{ClO}_4)_2$ exhibits the highest MS1 thermal stability and that MS1 can be photogenerated by blue light up to 230 K

using a continuous-wave (CW) light source for irradiation, and even at room temperature when using pulsed laser irradiation (Kostin *et al.*, 2018; Mikhailov *et al.*, 2019). We also showed that the thermal stability of MS2 is essential for the room-temperature generation of MS1, as the GS to MS1 excitation occurs via MS2 as an intermediate state (Mikhailov *et al.*, 2019). Accordingly, the aim of the current study is to improve the thermal stability of MS1 and MS2, using fluorine as a *trans*-to-NO ligand, by the synthesis of *trans*- $[\text{RuNO}(\text{NH}_3)_4\text{F}]\text{SiF}_6$, which crystallizes in a non-centrosymmetric space group. The structure of the complex is thoroughly analysed using X-ray diffraction (XRD) and SH generation. The properties and generation conditions of MS1 and MS2 are investigated by XRD, IR and UV–Vis spectroscopy and calorimetry. The NLO properties of GS are investigated in detail and an attempt is made to measure the changes induced by photo-generation of MS1 at room temperature.

2. Experimental

2.1. Synthesis of *trans*- $[\text{RuNO}(\text{NH}_3)_4\text{F}]\text{SiF}_6$

The synthesis of *trans*- $[\text{RuNO}(\text{NH}_3)_4\text{F}]^{2+}$ was performed in an analogous manner to that of the *trans*- $[\text{RuNO}(\text{py})_4\text{F}]^{2+}$ complex from our previous work (Kostin *et al.*, 2018). *trans*- $[\text{RuNO}(\text{NH}_3)_4\text{OH}]\text{Cl}_2$ (585 mg) was dissolved in concentrated HF (10 ml, 40%) and heated in a closed polypropylene vessel for 30 h at 363 K. The solution was then evaporated in air to dryness, resulting in a yellow residue. A few portions (3–5 ml) of diethyl ester were added to the solid in order to remove possible residual hydrofluoric acid. A yellow powder (604 mg) with presumed formula *trans*- $[\text{RuNO}(\text{NH}_3)_4\text{F}](\text{H}_n\text{F}_{n+1})_2$ was obtained. Single crystals of *trans*- $[\text{RuNO}(\text{NH}_3)_4\text{F}]\text{SiF}_6$ were obtained by dissolving this product, *trans*- $[\text{RuNO}(\text{NH}_3)_4\text{F}](\text{H}_n\text{F}_{n+1})$, in water in a glass tube. The yield of *trans*- $[\text{RuNO}(\text{NH}_3)_4\text{F}]\text{SiF}_6$ is $\sim 90\%$.

Spectroscopic analysis: IR bands at room temperature (cm^{-1}): 3328, 3228 [$\nu(\text{C}-\text{H})$], 1899 [$\nu(\text{NO})$], 737, 698 [$\nu(\text{Si}-\text{F})$], 1668, 1608, 1566, 1324, 1302 and 870 (amine vibrations). Elemental analysis for $\text{N}_5\text{H}_{12}\text{O}_7\text{F}_7\text{Si}_1\text{Ru}_1$, calculated/found (%): H 3.4/3.6, N 19.4/19.7, F 36.9/37.2. The powder XRD pattern of the bulk sample corresponds to the theoretical pattern calculated from the crystal structure determined by single-crystal XRD (Fig. S1 in the supporting information).

2.2. Single crystal X-ray diffraction

One single crystal of *trans*- $[\text{RuNO}(\text{NH}_3)_4\text{F}]\text{SiF}_6$ was selected and measured on a Rigaku Oxford Diffraction SuperNova four-circle diffractometer equipped with a molybdenum microfocus source ($\text{Mo K}\alpha$, $\lambda = 0.71073 \text{ \AA}$) and an Atlas CCD detector. An Oxford Cryosystems Cryostream nitrogen blower was used to maintain the sample temperature at 100 K. After measuring the ground state (GS), the same single crystal was irradiated for 120 min by a 405 nm 360 mW LED at 100 K in order to measure the photoinduced state. The light of the LED was collimated using an anti-reflection-coated aspheric condenser lens (COP1-A from Thorlabs),

yielding a homogenous spot of about 20 mm diameter at a distance of 150 mm. The crystal, of size $0.157 \times 0.104 \times 0.085$ mm, was centred on this spot and homogenous illumination was ensured by rotating the crystal by 90° every 30 min. The GS and photoinduced structures (corresponding to a mixture of GS and MS1) were solved using *OLEX2* (Dolomanov *et al.*, 2009) with the *olex2.solve* (Bourhis *et al.*, 2015) structure solution program using charge flipping, and refined with the *olex2.refine* (Bourhis *et al.*, 2015) refinement package using Gauss–Newton minimization. The GS structure of *trans*-[RuNO(NH₃)₄F]SiF₆ has been deposited with the CCDC with refcode 1910521. Data-collection and refinement parameters are given in Table S1.

2.3. Hirshfeld surface analysis

The Hirshfeld surfaces were calculated using *Crystal Explorer* (Hirshfeld, 1977; Spackman & Jayatilaka, 2009; Turner *et al.*, 2017). This program allows the normalized contact distance d_{norm} to be mapped onto the generated Hirshfeld surface. It is customary to map d_{norm} using a red–white–blue scheme, where red denotes close intermolecular contacts (negative d_{norm}), blue denotes longer contacts (positive d_{norm}) and white denotes intermolecular contacts equal to the van der Waals radii of atoms in contact ($d_{\text{norm}} = 0$). It is possible to obtain two-dimensional plots (fingerprint plots) from the surfaces mapped with d_{norm} values. Such plots are an invaluable asset in intermolecular interaction analysis since they serve as an executive summary of the quantity, nature and type of all intermolecular interactions at the same time.

2.4. Powder X-ray diffraction

Powder X-ray diffraction patterns were recorded using a PANalytical X'Pert PRO diffractometer equipped with a Cu X-ray tube, a Ge(111) incident-beam monochromator ($\lambda = 1.5406$ Å) and an X'Celerator detector.

2.5. IR and UV–Vis spectroscopy

IR spectroscopy measurements with irradiation were performed using a Nicolet 5700 FT–IR spectrometer with a resolution of 2 cm^{-1} in the range $400\text{--}4000 \text{ cm}^{-1}$. The sample was ground, mixed with KBr and pressed into pellets. The KBr pellets were bonded by silver paste onto the cold finger of a closed-cycle cryostat (Oxford Optistat V01) and irradiated by an LED through KBr windows with light of different wavelengths in the range $300\text{--}940 \text{ nm}$ and $10\text{--}400 \text{ mW}$ optical power (Thorlabs L and LP series). The cryostat allows control of the temperature in the range $9\text{--}320 \text{ K}$.

UV–Vis spectra were recorded using transparent KBr pellets with the complex by a Varian CARY 4000 spectrometer. Transparent pellets were prepared as for the IR measurements. Low-temperature measurements were performed using the same cryostat as for the IR measurements, except that the KBr windows were exchanged for standard borosilicate glass windows. The baseline was measured using the same diaphragm with a KBr pellet, which can be mounted on the cryostat sample holder.

2.6. Differential scanning calorimetry

Differential scanning calorimetry (DSC) experiments were performed on a Mettler–Toledo DSC1 instrument equipped with a high-sensitivity DSC HSS8 sensor. The sample ($\sim 5 \text{ mg}$ of the powder) was homogeneously spread in a standard aluminium crucible ($40 \mu\text{l}$), such that it formed a thin layer covering the whole surface of the crucible.

For MS1 generation, irradiation of GS was performed at 143 K for 40 min through a glass window, using LED light at 405 nm (Thorlabs M405LP1-C1) and with a light intensity of 360 mW . MS2 was generated under the same conditions by first irradiating at 405 nm for 40 min using 360 mW , followed by irradiation at 940 nm and 200 mW (Thorlabs M940L3-C2) for 60 min . To detect the enthalpy release during thermal relaxation of the metastable states, the sample was then heated from 143 to 353 K at a heating rate of 9 K min^{-1} . As a reference measurement the sample was measured using the same protocol but without light irradiation. The experimental data were processed using the Netzsch Proteus analysis software.

2.7. NLO properties

Single crystals of *trans*-[RuNO(NH₃)₄F]SiF₆ were ground in a mortar and pressed into a powder pellet as described by Kijatkin *et al.* (2017). For comparison, the same procedure was performed using magnesium-doped lithium niobate (LiNbO₃:Mg) nanoparticles (mean particle size $d \simeq 90 \text{ nm}$). Creating small-scale crystallites allows a loosening of the phase-matching conditions typically required for observing NLO signals. Spectrally tunable ultrashort laser pulses ($\tau \simeq 50 \text{ fs}$) at a pulse repetition rate of 1 kHz were obtained by a regeneratively amplified femtosecond oscillator (Astrella HE+ Coherent) equipped with an optical parametric amplifier (TOPAS Prime, Light Conversion). The incident laser pulses were directed onto the sample at a small angle of incidence ($\sim 30^\circ$). Diffusely backscattered radiation was collected and spectrally resolved using a glass fibre placed perpendicular to the sample surface, which was attached to a combination of a spectrograph and a CCD camera (IsoPlane SCT320 and PIXIS:2KBUV, Princeton Instruments). Parallel population of the metastable states was achieved using a 405 nm CW laser as a pump light source, irradiating the sample at a similar angle of incidence, thereby forming a symmetric beam geometry with respect to the sample surface. The intensity of both beams was regulated via neutral density filters. Backscattered pump radiation was attenuated before entering the spectrometer by a longpass filter (ZUL0422, Asahi Spectra).

2.8. Pump–probe transient absorption spectroscopy

The optical pump system consists of a Surelite II-10 Nd–YAG pulsed laser equipped with an optical parametric oscillator (OPO, model SLOPO+). The system delivers laser pulses of $3\text{--}5 \text{ ns}$ duration at a frequency of 10 Hz . The OPO was tunable in the range $400\text{--}700 \text{ nm}$. The laser beam was directed onto the sample position (the complex in a KBr pellet) using a series of silver-coated mirrors and was precisely adjusted and

focused through appropriate lenses ($f = 100, 200$ or 300 mm) to illuminate the sample uniformly (*i.e.* the beam diameter was larger than the sample). For the transient absorption measurement, a CW laser at 532 nm wavelength was used to probe the light-induced absorption. The probe beam was focused by a lens ($f = 300$ mm) onto the sample position such that the probe beam diameter was smaller than the pump beam diameter. Its intensity could be adjusted by a $\lambda/2$ waveplate and a polariser from a few microwatts to a few milliwatts. The probe light was detected by a 200 MHz Si-Pin diode from Femto Messtechnik GmbH. The voltage at the output of the detector was sampled using a 1.5 GHz oscilloscope (LeCroy WavePro 715Zi). The trigger was obtained directly from the laser (with a delay of 10 ns with respect to the arrival of the pump beam on the sample position). In order to block the pump light (410 nm), two interference filters at 532 nm (width of 5 nm) were mounted in front of the photodiode. The transient absorption signal was recorded in single-shot mode and averaged over 20 pump–probe cycles.

2.9. Elemental analysis

The elemental content of $trans$ -[RuNO(NH₃)₄F]SiF₆ (C, H, N) was determined using a Vario Microcube analyser. The fluorine content was determined after sample combustion by the Shoniger technique with an alkaline absorption liquid, by the spectrophotometric method with a lanthanum/alizarin complexone and by the potentiometric method with a fluorine-selective electrode. The discrepancy between the different methods did not exceed 0.1% .

3. Results and discussion

3.1. Synthesis and structural description

Heating $trans$ -[RuNO(NH₃)₄OH]Cl₂ with hydrofluoric acid results in the substitution of the OH[−] ligand by a fluoride anion. Conversion of the reaction was monitored by taking IR spectra of the resulting solid at different HF treatment times at

Table 1

Selected bond distances and angles (Å, °) in $trans$ -[RuNO(NH₃)₄F]SiF₆.

Distance	Distance	Angle			
Ru1–N5	1.719 (2)	Si1–F2	1.678 (2)	Ru1–N5–O1	175.9 (2)
N5–O1	1.144 (2)	Si1–F3	1.713 (2)	F1–Ru1–N5	177.2 (1)
Ru1–F1	1.938 (1)	Si1–F4	1.674 (2)	N1–Ru1–F1	85.2 (1)
Ru1–N1	2.091 (2)	Si1–F5	1.681 (2)	N2–Ru1–F1	87.1 (1)
Ru1–N2	2.098 (2)	Si1–F6	1.686 (1)	N3–Ru1–F1	85.9 (1)
Ru1–N3	2.092 (2)	Si1–F7	1.661 (1)	N4–Ru1–F1	85.9 (1)
Ru1–N4	2.083 (2)				

363 K. After heating for 30 h, the $\nu(\text{NO})$ stretching vibration of the precursor complex (1847 cm^{−1}) disappeared completely and a new $\nu(\text{NO})$ band at 1875 cm^{−1} arose in the IR spectrum. In the next step, the resulting yellow crystalline powder with presumed formula $trans$ -[RuNO(NH₃)₄F](H_{*n*}F_{*n+1*})₂ was dissolved in water in a glass tube, leading to the formation of $trans$ -[RuNO(NH₃)₄F]SiF₆ single crystals. In an earlier report on the synthesis of $trans$ -[RuNO(NH₃)₄F]²⁺ (Sinitzyn *et al.*, 1989), the precursor complexes $trans$ -[RuNO(NH₃)₄OH]-(NO₂)₂ or K₂[RuNOF₅]·H₂O were heated with molten NH₄HF₂ at 473 K for ~ 1 h in a platinum melting pot. The treatment of the precursor in these aggressive conditions indicates the high thermal stability of the $trans$ -[RuNO(NH₃)₄F]²⁺ cation. The final yield of the product was not mentioned in that report, but a few crystals of $trans$ -[RuNO(NH₃)₄F]SiF₆ were obtained.

The complex $trans$ -[RuNO(NH₃)₄F]SiF₆ crystallizes in the non-centrosymmetric space group Pn . The cell parameters are given in Table S1. The asymmetric unit contains two molecular ions, the [RuNO(NH₃)₄F]²⁺ cation and the SiF₆^{2−} anion, both in a distorted octahedral configuration [Fig. 1(a)]. The distances in the F–Ru–N–O fragment are Ru–NO = 1.719 (2) Å, N–O = 1.144 (2) Å and Ru–F = 1.938 (1) Å (Table 1). The angles in the F–Ru–N–O fragment are close to linear: Ru1–N5–O1 = 175.9 (2)° and F1–Ru1–N5 = 177.2 (1)°. While the bond distances Ru–N1 and Ru–N3 of the amine ligands *trans* to each other are equal [2.092 (2) Å],

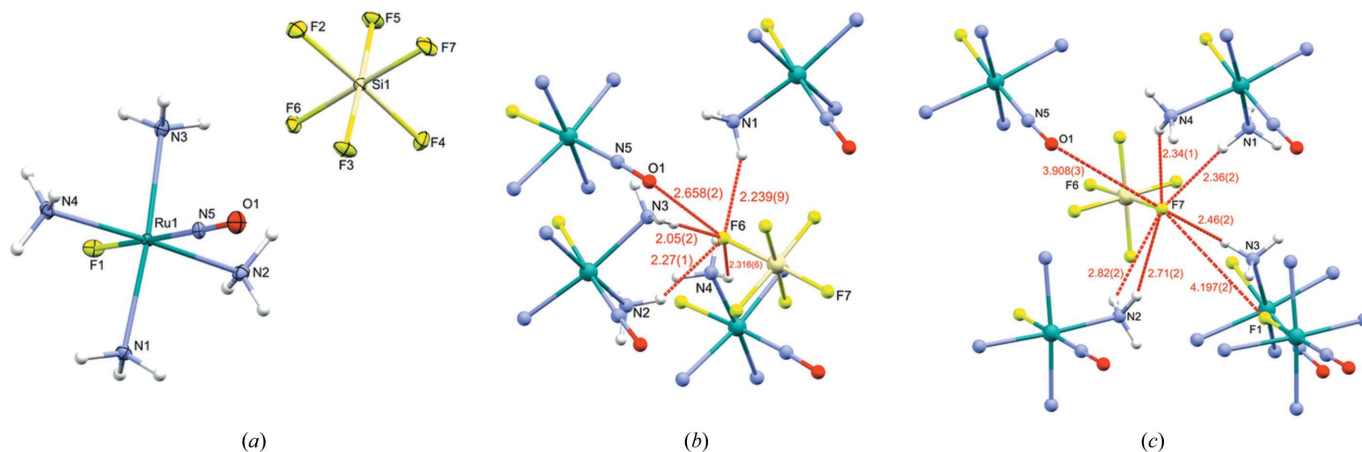


Figure 1

(a) The structure of the $trans$ -[RuNO(NH₃)₄F]SiF₆ complex. (b) and (c) The intermolecular contacts (Å) of F6 and F7. Ellipsoids in panel (a) represent anisotropic displacement parameters at the 50% probability level. Spheres in panels (b) and (c) are of arbitrary radii. Most of the H atoms in panels (b) and (c) have been removed for clarity.

the other two bond distances Ru–N2 and Ru–N4 exhibit a length difference of 0.015 (2) Å. The difference is due to packing effects as a consequence of the different involvement of the amine ligands in hydrogen bonds with the F atoms of the hexafluorosilicate anion. These hydrogen bonds, alongside the halogen bonds, are also responsible for the almost-parallel alignment of the molecular dipoles, resulting in a non-centrosymmetric structure. In the following we discuss these important intermolecular interactions in more detail using Hirshfeld surface analysis.

The Hirshfeld surface analysis reveals an abundance of hydrogen bonds between the amino groups of the cation and the fluoride atoms of the SiF_6^{2-} anion (Figs. 2 and S2). For the most part, individual bonds are reasonably strong (average H...F distance 2.170 Å, range 2.024–2.364 Å, sum of van der Waals radii 2.66 Å, average N–H...F angle 158.4°, range 145.3–173.4°). An average of two hydrogen bonds per F atom and several weaker contacts distort both octahedra (Table 1).

Reciprocal contacts are found on the Hirshfeld surface of the $\text{trans}[\text{RuNO}(\text{NH}_3)_4\text{F}]^{2+}$ cation. One intense or two moderate red spots are noticeable near almost every H atom, indicating the existence of regular and bifurcated hydrogen bonds. The remaining F ligand, which is bound to Ru, shows similar patterns of intermolecular contacts [Figs. 2 and S2(b)].

The nitrosyl ligand has a potential for both hydrogen and halogen bonds. There is a wealth of evidence for halogen bonds between F6 and O1 [Figs. 1(b), 1(c), S2(c) and S2(f)]. The F6...O1 distance is 2.658 Å (sum of van der Waals radii 2.96 Å), while the Si1–F6...O1 and F6...O1–N5 angles are 170.33° and 171.50°, respectively. Furthermore, this halogen bond has a profound impact on the *trans* (to F6) ligand F7, which has the shortest Si–F7 bond length of all the fluoride ligands. There is less evidence for hydrogen bonds between the amine ligands and O1 [Fig. S2(d)]; these are weak hydrogen bonds with shallow angles at best.

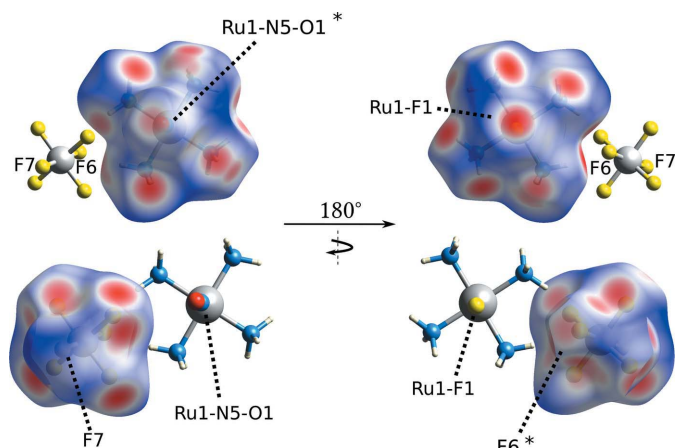


Figure 2
Three-dimensional Hirshfeld surface maps, coloured by d_{norm} in the range 0.5–1.5 Å. (Left) Front view and (right) back view. Regions coloured red and marked with an asterisk (*) indicate F6...O1 halogen bonds. Other red regions indicate N–H...F bonds.

3.2. Investigations of metastable states

3.2.1. Spectroscopic and structural studies. IR spectroscopy is an extremely sensitive technique for detecting a bond-linkage change. The NO stretching vibration $\nu(\text{NO})$ is a particularly useful fingerprint for the identification of nitrosyl linkage isomers (Mikhailov *et al.*, 2019). Concerning the spectrum of GS, the $\nu(\text{NO})$ band has a maximum at 1902 cm^{-1} with a shoulder at 1910 cm^{-1} at 10 K. Light irradiation of GS in the range 300–500 nm generates MS1, characterized by its $\nu(\text{ON})$ band with a maximum at 1769 cm^{-1} (Fig. 3). The $\nu(\text{ON})$ band of MS1 exhibits a shift of 133 cm^{-1} to lower energy compared with the $\nu(\text{NO})$ band of GS, which is typical for ruthenium nitrosyl compounds (Schaniel, Cormary *et al.*, 2007; Kostin *et al.*, 2015, 2017, 2018). The most efficient wavelengths for inducing the GS-to-MS1 transfer are in the range 405–420 nm (Fig. S3).

Further signatures of the MS1 isomer formation are the bands appearing at 577, 532 and 466 cm^{-1} , which we tentatively assign to the $\nu(\text{Ru}-\text{O}_{\text{NO}})$ stretching mode, the $\delta(\text{Ru}-\text{O}-\text{N})$ deformation mode and the $\nu(\text{Ru}-\text{F})$ stretching vibration, respectively. The appearance of these bands is accompanied by a decrease in the corresponding GS bands at 544, 503 and 473 cm^{-1} (Fig. S4). The assignment is made based on the literature data (Weidemann *et al.*, 1998). Again, the change in these low-energy vibrations upon MS1 formation is expected, as was shown for ruthenium nitrosyl complexes with *trans*-ligands $X = \text{F}^-$, OH^- (Kostin *et al.*, 2015, 2017, 2018).

Concerning the vibrations of the amine groups, the appearance of new $\delta(\text{NH}_3)$ bands of MS1 at 870 and 833 cm^{-1} and the corresponding decrease in the GS $\delta(\text{NH}_3)$ bands at 876, 854 and 848 cm^{-1} , as well as perturbations of the $\nu(\text{Ru}-\text{N}_{\text{NH}_3})$ bands in the 1550–1700 cm^{-1} range after irradiation, are evidence again that the whole structure (axial and planar ligands of the octahedral complex) adapts to the NO rearrangement.

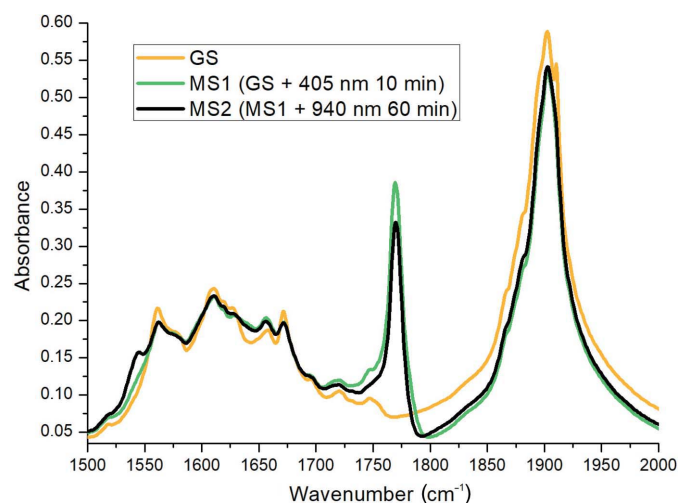


Figure 3
IR spectra at 10 K for the GS (orange line), GS+MS1 (green line) and GS+MS1+MS2 (black line).

By irradiation of MS1 with 940 nm light it is possible to generate the MS2 isomer $[\text{Ru}-(\eta^2\text{-NO})]$, *i.e.* irradiation in the near-IR induces the transfer of MS1 to MS2. The appearance of the MS2 isomer is characterized by the formation of the $\nu[\eta^2\text{-}(\text{NO})]$ band with a maximum at 1545 cm^{-1} . Compared with GS, the NO stretching vibration shifts to a significantly lower wavenumber by 357 cm^{-1} , which again is typical for the MS2 isomer (Schaniel, Cormary *et al.*, 2007; Kostin *et al.*, 2015). Moreover, a new band with a maximum at 561 cm^{-1} is detected, most probably corresponding to the $\delta(\text{Ru}-\text{N}-\text{O})$ deformation mode of MS2.

The populations of both MS are determined from the decrease in the area of the $\nu(\text{NO})$ GS band and amount to $\sim 10\%$ for MS1 and $\sim 3\%$ for MS2. Irradiation of both MS1 and MS2 in the range 505–810 nm leads to a transfer back to GS. A summary of the wavelength dependence of the GS–MS transformations under light exposure is given in Fig. S5. As will be detailed below, the photogeneration of MS1 occurs through a two-step process via the second metastable state MS2, *i.e.* $\text{GS} \rightarrow \text{MS2} \rightarrow \text{MS1}$, where MS2 is generated by a one-photon excitation. Any photon arriving within the lifetime of MS2 then induces the second step, $\text{MS2} \rightarrow \text{MS1}$, at the same wavelength.

In order to gain a better understanding of the population and depopulation processes of MS1 and MS2, the UV–Vis absorption spectra of *trans*- $[\text{RuNO}(\text{NH}_3)_4\text{F}]\text{SiF}_6$ in KBr before and after light irradiation were measured at 100 K (Fig. 4). GS exhibits a strong absorption from the UV up to 500 nm, whereas MS1 absorbs light over the whole measured range of 350–900 nm and has its lowest lying absorption band with a maximum around 550 nm (Fig. 4, inset). MS2, like MS1, absorbs over the entire measured range and exhibits an absorption maximum at 500 nm. Within the $\text{GS} \rightarrow \text{MS2} \rightarrow \text{MS1}$ generation scheme, GS can thus be excited to MS1 by irradiation in the range 405–420 nm, due to the strong absorption bands of GS and MS2 and a comparable less efficient

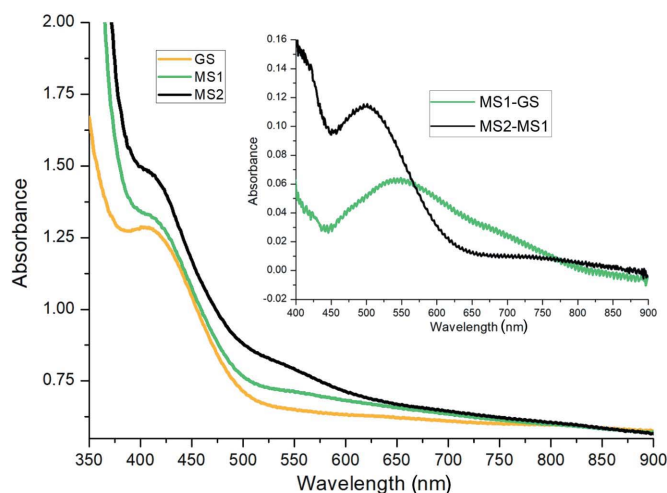


Figure 4 UV–Vis spectra for GS (orange line, before irradiation), GS+MS1 (green line, after 90 min of 405 nm irradiation of GS) and GS+MS1+MS2 (black line, after 60 min of subsequent 940 nm irradiation of MS1) at 100 K. (Inset) MS1 and MS2 spectra after GS and MS1 subtraction, respectively.

absorption of MS1 in this spectral range. Above 450 nm, the MS1 absorption increases and, as a consequence, the cross section of the MS1-to-GS reaction increases, which results in a decrease in the population of MS1 in the case of excitation wavelengths of 450 nm and above (Fig. S3). Furthermore, since MS1 and MS2 exhibit significant absorption in the 450–810 nm spectral range, light irradiation in that region might lead to a transfer of MS1 and MS2 back to GS. IR exposure (940 nm) of MS1 results in the formation of MS2, but also in a slow back-transfer to GS, which indicates that the cross section of the $\text{MS1} \rightarrow \text{MS2}$ reaction in this spectral region is higher than for the $\text{MS1} \rightarrow \text{GS}$, $\text{MS2} \rightarrow \text{GS}$ or $\text{MS2} \rightarrow \text{MS1}$ transformations.

While identification of the two linkage isomers MS1 and MS2 in nitrosyl compounds using IR spectroscopy is well established, a direct confirmation of the structural changes by X-ray diffraction (XRD) is desirable. However, due to the relatively low populations of MS1 (10%) and MS2 (3%) and the significant spatial overlap of the different linkage-isomer configurations (especially GS and MS1), the structural analysis has to be performed with care. We restrict the photocrystallographic investigations to the case of MS1.

Initial model-independent evidence for NO isomerization is obtained by analysis of photodifference maps, an adequate tool for the study of structural changes even in the case of low populations (Schaniel *et al.*, 2018). The same single crystal used for the GS structure determination was used for MS1 data collection after irradiation at 405 nm (360 mW LED for 120 min). The crystal colour changes from bright yellow to pale yellow after light exposure (Fig. S6). The unit-cell parameters change from 6.7036 (4) to 6.7242 (4) Å and from 10.1296 (7) to 10.1347 (7) Å for *a* and *c*, respectively, while *b* changes only slightly from 7.4260 (4) to 7.4249 (4) Å (Table S1). Note that the F–Ru–N–O axis is almost perpendicular to the *b* axis, so the small increase in *a* and *c* might be expected from the lengthening of the Ru–O distance in the Ru–ON (MS1) bond compared with the Ru–N distance in Ru–NO (GS). The photodifference map is the Fourier transform of the difference between the structure factors of the photoexcited structure (GS+MS1) and the structure before irradiation (GS) (Schaniel *et al.*, 2018). For the present case, the photodifference map (Fig. 5) is drawn in the Ru–N–O plane and shows a significant lack of electron density around atom O1. Near atom N5 some diffuse excess electron density is observed, but it is at the same level as the noise. This observation is typical for the case of a 180° NO isomerization, since the ‘electron-rich’ O atom in MS1 occupies the position of the N atom and vice versa. Therefore, in MS1 the electron density at the O1 position of GS is reduced, while at the N5 position it is increased. We also observe a change in electron density on the Ru position, which is due to a small displacement of Ru in MS1 compared with GS.

Having unambiguously established the presence of the MS1 isomer, we discuss in the following an approach to refine a structural model for MS1. In the first step, a structure refinement of GS+MS1 is performed using a single structural configuration to model the experimental data, one assuming a

100% Ru–NO configuration as for GS, and one using a 100% Ru–ON configuration as one might expect if the GS to MS1 conversion were complete. Atomic distances for the structures obtained after these two refinements are shown in Table 2. Regardless of the model used (Ru–NO or Ru–ON), the distance between Ru and the nitrosyl ligand increases by 0.02–0.03 Å. Residual electron-density maps of both structure refinements are shown in Fig. S7. For the model assuming the GS Ru–NO configuration, no excess or lack of electron density around the nitrosyl ligand is observed. In the case of the model with an Ru–ON configuration, significant residuals are observed. There is a lack of electron density near the N atom and an excess of electron density around the O atom of the nitrosyl ligand. The lack of electron density indicates that the N atom should be substituted by a more electron-rich atom, while the excess of electron density indicates that the O atom should be substituted by a less electron-rich atom. Since the model with Ru–NO yields a better fit of the GS+MS1 structure and the elongation of the Ru–(NO) distance is only 0.02–0.03 Å, we can conclude that the population of the Ru–ON isomer is significantly lower than that of the Ru–NO isomer, in agreement with the spectroscopic results. For comparison, in the $K_2[RuNO(NO_2)_4OH]$, $[RuNO(py)_2(NO_2)_2OH]$, $[RuNO(py)_4Cl](PF_6)_2 \cdot 0.5H_2O$ and $[RuNO(py)_4F](ClO_4)_2$ ruthenium nitrosyl complexes, the elongation of the Ru–(NO) bond distance from GS to MS1 was 0.1 (1) Å (Fomitchev & Coppens, 1996; Cormary *et al.*, 2009; Kostin *et al.*, 2015; Mikhailov *et al.*, 2019).

In the second step, the excited structure is modelled using a split model for the NO group, *i.e.* a mixture of the two configurations Ru–ON and Ru–NO (Table 2). In the light of

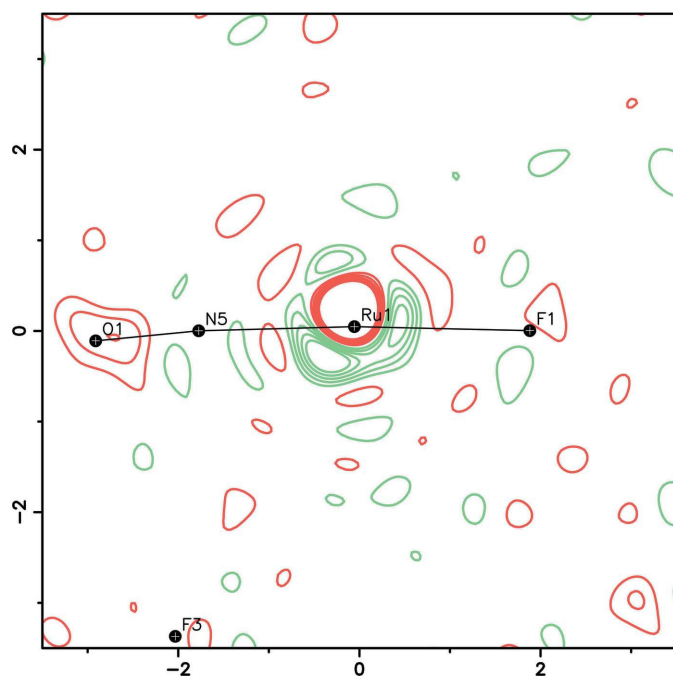


Figure 5
A two-dimensional photodifference map between the photoinduced state (GS+MS1) and GS. Residual electron-density contours are $0.35 e \text{ \AA}^{-3}$. A lack of electron density is shown by red contours and an excess by green contours.

Table 2
Selected bond distances and angles (\AA , $^\circ$) for GS and for the three models of GS+MS1.

Distance/angle	GS+MS1			
	GS Ru–NO	GS (100%) Ru–NO	MS1 (100%) Ru–ON	GS/MS1 (80/20%) split model Ru–NO/Ru–ON
Ru1–N5	1.719 (2)	1.740 (2)		1.731 (3)
Ru1–O1			1.747 (2)	1.789 (5)
N5–O1	1.144 (2)	1.148 (2)	1.141 (2)	1.157 (4)/1.13 (1)
Ru1–F1	1.938 (1)	1.936 (1)	1.939 (2)	1.936 (1)
Ru1–N1	2.091 (2)	2.090 (3)	2.093 (3)	2.091 (2)
Ru1–N2	2.098 (2)	2.103 (3)	2.099 (3)	2.102 (3)
Ru1–N3	2.092 (2)	2.092 (3)	2.088 (3)	2.092 (3)
Ru1–N4	2.083 (2)	2.082 (3)	2.083 (3)	2.083 (3)
Si1–F2	1.678 (2)	1.684 (3)	1.686 (3)	1.684 (3)
Si1–F3	1.713 (2)	1.712 (2)	1.713 (2)	1.712 (2)
Si1–F4	1.674 (2)	1.677 (3)	1.676 (3)	1.677 (3)
Si1–F5	1.681 (2)	1.686 (2)	1.684 (2)	1.686 (2)
Si1–F6	1.686 (1)	1.690 (2)	1.687 (2)	1.690 (2)
Si1–F7	1.661 (1)	1.664 (2)	1.669 (2)	1.664 (2)
Ru1–N5–O1	175.9 (2)	175.7 (2)		173.0 (4)
Ru1–O1–N5			175.4 (2)	165 (1)
F1–Ru1–N5	177.2 (1)	177.2 (1)		177.9 (2)
F1–Ru1–O1			176.8 (1)	173.9 (3)
N1–Ru1–F1	85.2 (1)	85.4 (1)	85.8 (1)	86.5 (1)
N2–Ru1–F1	87.1 (1)	87.5 (1)	87.5 (1)	87.5 (1)
N3–Ru1–F1	85.9 (1)	86.6 (1)	86.4 (1)	85.5 (1)
N4–Ru1–F1	85.9 (1)	86.1 (1)	86.1 (1)	86.1 (1)

our conclusions above and the fact that the population of MS1 is 10% from the IR measurements, we have constrained the occupancy of MS1 to 20%. In the case of a refinement with less than 20% of MS1, the MS1 displacement parameters of the nitrosyl atoms become non-positive definite even when using an isotropic refinement. Using this constrained model, we obtain an Ru–ON bond length of 1.789 (5) Å, which is 0.07 (1) Å longer than in the GS structure. The Ru–O–N angle changes to 165 (1)°. All other bond distances in the GS+MS1 structure are the same as in GS to within the limit of error. Since the population of the Ru–ON isomer is only 10–20%, the accuracy of the structural parameters obtained from the refinement of the structure of MS1 is limited, as discussed in the literature (Cormary *et al.*, 2009; Kostin *et al.*, 2015; Mikhailov *et al.*, 2019). For example, the largest change in the bond lengths after blue-light irradiation is the elongation of the Ru–ON bond by 0.1 (1) Å, which can be unambiguously refined only in the case of high populations of the Ru–ON state. In case of an MS1 population of less than 50%, the structural parameters of MS1 in the presence of GS should be interpreted with care. Simulations showed that typical errors on the Ru1–O1 distance are of the order of 0.03 Å. For an in-depth discussion of the correlation between population and structural and anisotropic displacement parameters we refer the reader to the work of Cormary *et al.* (2009). All in all, we can conclude that MS1 of *trans*- $[RuNO(NH_3)_4F]SiF_6$ represents the typical structural behaviour of the isonitrosyl isomer in the nitrosyl ruthenium family.

3.2.2. Thermal stability of metastable states. For potential applications the thermal stability of MS1 and MS2 is essential. We determined the energy barriers of the MS1-to-GS and

Table 3
Kinetic parameters for the MS1 → GS reaction.

<i>Trans</i> complex	E_a (eV)	k_0 (s ⁻¹)	T_d (K)	$T_{\max \text{ of DSC}}^\dagger$ (K)	Reference
[RuNO(en) ₂ Br]Cl ₂	0.53	5.2×10^8	229	≈250‡	Ookubo <i>et al.</i> (1996)
[RuNO(en) ₂ Cl]Cl ₂	0.69	1.7×10^{11}	246	≈270‡	Ookubo <i>et al.</i> (1996)
[RuNO(NH ₃) ₄ OH]Cl ₂	0.91	6×10^{14}	258	≈280	Schaniel <i>et al.</i> (2005)
[RuNO(NH ₃) ₄ F]SiF ₆	1.01	2.6×10^{14}	292	≈310	Present work
[RuNO(py) ₄ Br](PF ₆) ₂				≈210	Coppens <i>et al.</i> (2002)
[RuNO(py) ₄ OH](PF ₆) ₂				≈220	Coppens <i>et al.</i> (2002)
[RuNO(py) ₄ Cl](PF ₆) ₂	0.70	2×10^{12}	231	≈250	Schaniel <i>et al.</i> (2007)
[RuNO(py) ₄ F](ClO ₄) ₂	1.02	7.9×10^{14}	289	≈310	Kostin <i>et al.</i> (2018)

[†] $T_{\max \text{ of DSC}}$ is the temperature on the maximum of the DSC curve. [‡] Approximate values, since in the work of Ookubo *et al.* (1996) the IR technique was used to determine the kinetics. The approximation was made based on the observation that the difference between T_d and $T_{\max \text{ of DSC}}$ is typically ~20 K. Note that $T_{\max \text{ of DSC}}$ depends on the heating rate (Kostin *et al.*, 2015).

MS2-to-GS reactions using DSC. The kinetic parameters of the exothermic reactions (activation energies E_a and frequency factors k_0) were calculated using the first-order kinetic equation

$$dH/dt = H_{\text{tot}}(1 - \alpha)k_0 \exp[-E_a/(RT)], \quad (1)$$

where dH/dt is the heat-flow rate, H_{tot} is the total reaction enthalpy, α is the conversion, R is the universal gas constant and T is the temperature. The DSC curves are shown in Fig. S8. According to the fit, E_a and $\log k_0$ for the MS1→GS and MS2→GS reactions are 97.4 (3) kJ mol⁻¹ and 14.42 (4), and 59.0 (5) kJ mol⁻¹ and 12.0 (1), respectively.

A useful parameter to compare the thermal stability of MS of different complexes is the so-called decay temperature T_d (Morioka *et al.*, 2000), which is the temperature calculated for a value of the rate constant of $k = 10^{-3} \text{ s}^{-1}$ from the Arrhenius law,

$$k = k_0 \exp[-E_a/(RT)]. \quad (2)$$

The T_d values for MS1 and MS2 are 292 and 206 K, respectively. The T_d for MS1 in *trans*-[RuNO(NH₃)₄F]SiF₆ is the highest decay temperature known up to now (see Table 3), thereby confirming that the fluorine ligand *trans* to NO has a positive effect on the thermal stability (Yamaletdinov & Zilberberg, 2017; Kostin *et al.*, 2018). In order to illustrate the influence of the *trans*-to-NO ligand on the thermal stability of MS1, Table 3 summarizes the kinetic parameters of the MS1→GS reaction for a series of complexes with the same ligand environment (NH₃, ethylenediamine and pyridine in the equatorial position) and charge. Earlier, the influence of the *trans*-to-NO ligand in *trans*-[RuNO(NH₃)₄X]²⁺ on the activation energy of the MS1→GS reaction was investigated by density functional theory (DFT) calculations (Yamaletdinov & Zilberberg, 2017). According to that work, E_a increases in the sequence $X = \text{SH}^-, \text{OH}^-, \text{Cl}^-, \text{F}^-$ and equals 0.66, 0.97, 1.04 and 1.24 eV, respectively. A discussion of the difference between the calculations and the experimental data is beyond the scope of the present study, but one can state that the same trends are observed by both approaches and the complexes with $X = \text{F}^-$ show the highest E_a and T_d for the MS1→GS transformation.

3.2.3. Generation of MS1 and MS2 at room temperature. The temperature at which MS1 can be populated depends

strongly on the MS2 lifetime due to the two-step isomerization mechanism GS→MS2→MS1, *i.e.* increasing the lifetime of MS2 will lead to an increase in the temperature at which MS1 can be populated (Mikhailov *et al.*, 2019). Since *trans*-[RuNO(NH₃)₄F]SiF₆ and *trans*-[RuNO(py)₄F](ClO₄)₂ exhibit almost the same T_d of MS1 (292 and 289 K, respectively) but different T_d of MS2 (206 and 185 K, respectively; Kostin *et al.*, 2018), we expect to increase the temperature at which MS1 can be populated using CW light sources like LEDs (230 K for *trans*-[RuNO(py)₄F](ClO₄)₂; Mikhailov *et al.*, 2019).

The IR spectra of the *trans*-[RuNO(NH₃)₄F]SiF₆ complex recorded after 15 min of 405 nm irradiation (LED, 360 mW) at temperatures of 290, 295 and 300 K are shown in Fig. 6. After irradiation of GS at these temperatures, a band with a maximum at 1766 cm⁻¹ is clearly visible in the spectrum, corresponding to the $\nu(\text{ON})$ band characteristic of the MS1 isomer. The decay of this band at 300, 295 and 290 K occurs over ~300, ~700 and ~1300 s, respectively, which correspond to the lifetimes of MS1 calculated from the DSC measurements (353, 684 and 1357 s at 300, 295 and 290 K, respectively). The decay of the MS1 band is shown as an example for the measurement at 290 K in Fig. S9, together with a mono-

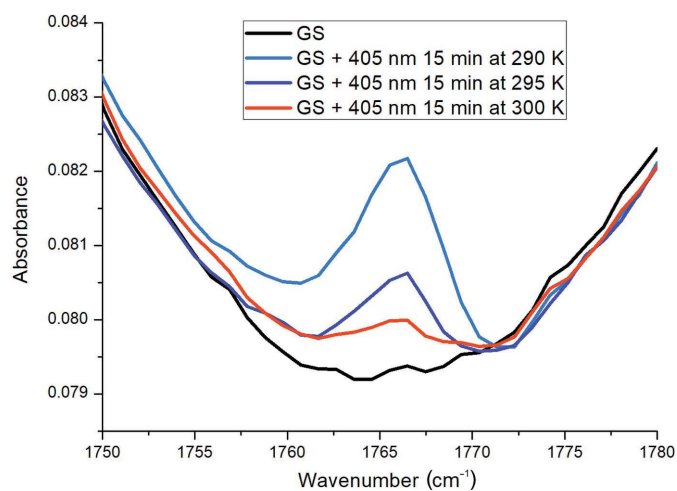


Figure 6
The generation of the MS1 isomer by 15 min of 405 nm 360 mW irradiation at different temperatures: 290 K (blue line), 295 K (purple line) and 300 K (red line). The populations of MS1 at these temperatures are 0.5, 0.4 and 0.2%, respectively.

exponential fit of the relaxation. Thus, for *trans*-[RuNO(NH₃)₄F]SiF₆, the photogeneration of MS1 using CW light sources is possible even at 300 K, which is a necessary prerequisite in view of potential applications, and an important improvement with respect to *trans*-[RuNO(py)₄F](ClO₄)₂, where MS1 photogeneration at 300 K was only achieved by pulsed-laser irradiation (Mikhailov *et al.*, 2019). This improvement is due to the increase in the activation energy of the MS2→GS reaction by 11.5 kJ mol⁻¹ (0.1 eV) from *trans*-[RuNO(py)₄F](ClO₄)₂ [$E_a(\text{MS2} \rightarrow \text{GS}) = 46.4 \text{ kJ mol}^{-1}$; Kostin *et al.*, 2018; Mikhailov *et al.*, 2019] to *trans*-[RuNO(NH₃)₄F]SiF₆ [$E_a(\text{MS2} \rightarrow \text{GS}) = 59.0 \text{ kJ mol}^{-1}$]. The increase in activation energy leads to an increased MS2 lifetime, which results in a higher probability of the MS2→MS1 reaction via the GS→MS2→MS1 mechanism.

Further support for this two-step mechanism of isomerization is obtained from transient nanosecond pump–CW probe spectroscopy at room temperature. The temporal decay of the light-induced absorption after pumping with a 410 nm laser pulse is shown in Fig. S10. The absorption decay is fitted by mono-exponential kinetics and characterized by a 13 (1) ms lifetime, corresponding to the MS2 state and its thermal decay process, which is in agreement with the calculated MS2 lifetime at $\approx 300 \text{ K}$. These findings show, again, that after excitation of the complex with a single laser pulse a small but measurable amount of the MS2 state can be populated, while long-term irradiation with a 405 nm LED allows the generation of MS1 by a sequential two-step photon absorption from GS to MS2 to MS1.

3.3. NLO properties – generation of the second and third harmonics

Our structural investigations of *trans*-[RuNO(NH₃)₄F]SiF₆ confirmed that it crystallizes in a non-centrosymmetric space group. The lack of an inversion centre should enable even-order harmonic generation, in particular second-harmonic (SH) generation. Using femtosecond pulses in the near-IR with peak intensities of the order of $3 \times 10^{14} \text{ W m}^{-2}$ (a time-averaged power of approximately 0.8 W cm^{-2}) reveals a remarkable harmonic emission, as shown in Fig. 7.

Because of the pronounced absorption in the blue spectral range, the fundamental wavelength was tuned between $\lambda = 1400$ and 1560 nm in order to shift both second and third harmonics further into the transmission window (see Fig. 4) for an unobstructed generation of harmonics, in particular of the third harmonic. Regardless of the selected wavelength, the observed SH emission intensity becomes of notable interest, exceeding that of a standard NLO material such as lithium niobate (LN) by a factor of approximately three. Simultaneously, the TH signal of *trans*-[RuNO(NH₃)₄F]SiF₆ is up to an order of magnitude weaker than for LN, which can be explained by an absorption band in the range of 400–550 nm. As a result, the harmonic ratio f_R , describing the polarity of the material and providing an accessible quantity for the characterization of second-order nonlinearities (Kijatkin *et al.*,

2017; Athmani *et al.*, 2019), is considerably higher for the ruthenium complex compared with LN.

In this context, it is worth discussing the potential origins of the remarkable nonlinear emission. The overall amplitude of the signal may partially stem from the different crystallite size, as it has been shown that the SH signal is sensitive to the particle volume (Knabe *et al.*, 2012; Kim *et al.*, 2013). However, this explanation does not fully suffice in elucidating the relative weakness of the TH peak, considering that, at the present length scales, it should increase with the particle volume as well. Because the second-order nonlinear susceptibility $\chi^{(2)}$ is composed of the individual hyperpolarizabilities β_i of the building blocks inside a volume element of the crystal (which likewise can be applied to higher orders; Chemla, 1980), a thorough look is required on the molecular level.

According to Akl *et al.* (2013), the molecular hyperpolarizabilities calculated from DFT for [Ru(NO)(*R*-terpyridine)Cl₂](PF₆) compounds are of the order of $\beta = \pm 5 \times 10^{-30} \text{ cm}^5 \text{ esu}^{-1}$, depending on the substituent *R* (NH₂, H or NO₂). Sakaguchi *et al.* (1989) reported values of $\beta = 70 \times 10^{-30} \text{ cm}^5 \text{ esu}^{-1}$ for derivatives of [Ru(tris(2,2′-bipyridine))] complexes. It is therefore reasonable to assume β values of the order of $10 \times 10^{-30} \text{ cm}^5 \text{ esu}^{-1}$ for *trans*-[RuNO(NH₃)₄F]SiF₆. Based on this assumption, we can rationalize the observed SH response compared with LiNbO₃. LiNbO₃ exhibits a β value of $21 \times 10^{-24} \text{ cm}^5 \text{ esu}^{-1}$ for particle diameters of 120 nm (Staedler *et al.*, 2012), which can be related to an average bulk nonlinear coefficient $\langle d \rangle = 4.8 \text{ pm V}^{-1}$, where $\langle d \rangle = \beta/V_p$ with V_p the volume of the (nano)particle (Le Dantec *et al.*, 2011). Despite the considerable difference of six orders of magnitude between these

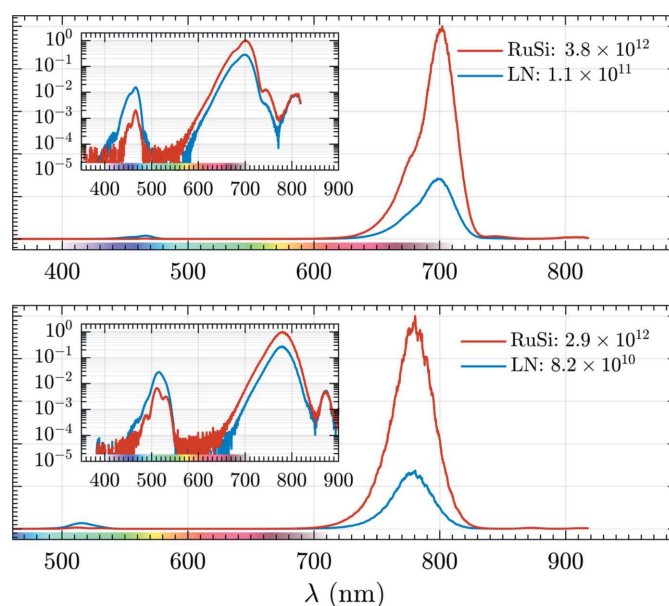


Figure 7
Harmonic emission spectra normalized to the maximum signal of *trans*-[RuNO(NH₃)₄F]SiF₆ (RuSi) and LiNbO₃:Mg (LN) at fundamental central wavelengths of (top) $\lambda = 1400 \text{ nm}$ and (bottom) $\lambda = 1560 \text{ nm}$. The insets display the same spectra on a logarithmic scale for better visibility of the third harmonic. Numerical values indicate the harmonic ratio f_R .

hyperpolarizabilities, the differing particle sizes for both materials may easily remedy the observed SH intensity difference which scales with the sixth power of the particle diameter (Kim *et al.*, 2013; Hsieh *et al.*, 2009). In fact, inspection of the prepared *trans*-[RuNO(NH₃)₄F]SiF₆ powder by optical microscopy shows particles with sizes between a few hundred nanometres and a few micrometres in diameter, thereby compensating for the lower β and improving the SH emission over LN nanoparticles.

Because of MS1 formation at room temperature after blue-light exposure, the possibility of changes in the harmonic emission intensity was investigated next. Furthermore, a time-resolved scan of the nonlinear emission for several minutes allows an assessment in terms of the photostability of the compound in the context of further applications. A selection of such measurements at a fundamental wavelength $\lambda = 1560$ nm is presented in Fig. 8.

Exposure at CW equivalent intensities of 1 W cm^{-2} (blue-light 405 nm, CW pump) and 0.8 W cm^{-2} (IR 1560 nm, femtosecond laser) yields a notable decrease in the SH intensity after a few minutes (see Fig. 8, top). Visual inspection after exposure reveals a considerable darkening of the sample surface, correlating with the significant SH signal decrease, especially during CW exposure, over time. Because of the pronounced UV/blue absorption band of the complex, a significant amount of energy is deposited in the sample, which exceeds heat-dissipation rates, thereby leading to irreversible

thermal damage. In fact, this behaviour is present even upon femtosecond pulse illumination, as shown for times $t \leq 85$ s. Potential causes include a non-negligible absorption at the fundamental wavelength or considerable absorption at the harmonics' wavelengths (*i.e.* 780 nm for the second harmonic and 520 nm for the third harmonic, respectively), as evident in Fig. 4.

As a consequence, the femtosecond IR pulse beam was attenuated to a level where temporally stable, yet significant, harmonic emission was observed for several minutes, as shown in Fig. 8 (middle), resulting in a mean power of 0.5 W cm^{-2} (peak intensity $2 \times 10^{14} \text{ W m}^{-2}$). At this rate, harmonic emission can easily be detected for a prolonged duration without any notable decrease in the conversion efficiency that would directly correlate with a darkening of the sample surface. Outside of the present investigations, this finding defines an upper limit in disparate areas of application, in particular where the ruthenium complex may be used as a contrast-enhancing agent. Naturally, providing there is sufficient external heat dissipation, a higher CW-equivalent intensity may be attained at no cost of material quality degradation. Vice versa, lower CW-equivalent intensities probably do not harm the sample at all; because of the (peak) intensity dependence of NLO effects on the fundamental wave, a reduction in the pulse repetition rate gives no decrease in the signal intensity per pulse. Thus, NLO emission can be further boosted by focusing, without increasing the radiant exposure by increased pulse-to-pulse delays.

A temporal scan of the SH emission upon population of MS1 by the CW laser at a lower intensity (0.1 W cm^{-2}) reveals a decrease in the nonlinear emission signal after pumping. However, thermal degradation due to the double exposure cannot be fully ruled out, as a slight darkening of the excitation spot is visible at the end of the series. Therefore, a definite answer with regard to a change in polarity upon switching from the ground to the metastable state cannot yet be provided using this method. The strength of such a signal change is determined decisively by both the level of metastable state population and the actual variation in the molecular hyperpolarizability β , which also depends on the non-nitrosyl ligands of the ruthenium complex and especially their donor–acceptor capability (Akl *et al.*, 2013).

Nevertheless, due to its strong SH emission, *trans*-[RuNO(NH₃)₄F]SiF₆ may be used in promising applications as a nonlinear emitter. Due to its low water solubility in particular, it is a potential candidate for (biomedical) imaging or detection.

4. Conclusions

Long-term treatment of the *trans*-[RuNO(NH₃)₄OH]Cl₂ precursor by HF allows the quantitative substitution of a hydroxyl ligand by a fluoride, indicating that the substitution reaction is kinetically accessible at ~ 373 K. Subsequent precipitation of the product by hexafluorosilicate yields the *trans*-[RuNO(NH₃)₄F]SiF₆ salt, crystallizing in the space group *Pn*. Analysis of the non-centrosymmetric structure of

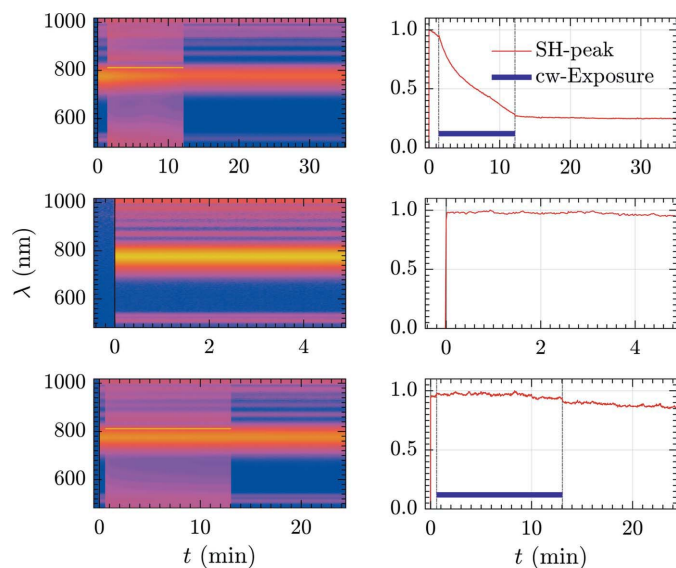


Figure 8

The evolution of (left) the emission spectrum and (right) the normalized emission intensity of the SH peak as a function of time. Sections of CW pump exposure in the right-hand plots have been marked. (Top) The emission at the maximum intensity of both IR and blue-light sources. (Middle) The medium intensity of the femtosecond laser source without the pump laser. (Bottom) The emission at medium intensity of both femtosecond and CW lasers. The sharp line visible in the top and bottom spectrotemporal plots at 810 nm is an artefact originating from the second-order diffraction signal of the pump laser. Similarly, the broadband signal appearing during the pumping process results from stray light from the CW laser inside the spectrometer.

trans-[RuNO(NH₃)₄F]SiF₆ by Hirshfeld surfaces reveals that H···F and F···O are the prevalent intermolecular interactions. These interactions result in an almost parallel alignment of the dipole moments of the [RuNO(NH₃)₄F]²⁺ cations, responsible for the observed NLO properties of the bulk material.

Thermal analysis of the metastable states shows that the increase in the MS2 lifetime leads to a higher probability of the MS2→MS1 reaction, and hence to a higher efficiency of the overall two-step photoisomerization GS→MS2→MS1. As a consequence, MS1 can be generated at 290–300 K using a blue-light LED as the irradiation source, thereby opening the possibility for CW-based optical applications at room temperature. On the other hand, the complex shows significant SH emission upon exposure to 1400–1560 nm femto-second pulses.

According to the Cambridge Structural Database (Groom *et al.*, 2016), there are at least 100 known octahedral ruthenium nitrosyl complexes which crystallize in a non-centrosymmetric space group. Hence, there are a large number of compounds with potentially interesting NLO properties, in particular SH emission.

Finally, our attempts to modify the emission of the nitrosyl ligand by photoisomerization (GS to MS1) at room temperature were inconclusive. In order to prove SH modification by nitrosyl photoisomerization, the MS1 population needs to be increased, which might be achieved by using other ruthenium nitrosyl compounds and/or working at low temperature.

Acknowledgements

We thank Sébastien Pillet for help with the calculation of the photodifference maps and Pierrick Durand of the PMD²X platform of IJB for performing the powder XRD measurements. We also thank the Federal Agency for Scientific Organizations for funding.

Funding information

Funding for this research was provided by: Comprehensive Program of Fundamental Research (grant No. 19-03-00594 A to Gennadiy Kostin); Campus France (bursary No. P730329G to Artem Mikhailov); PHC PROCOPE (grant No. 40539XA to Dominik Schaniel); Lorraine Université d'Excellence (grant No. ANR-15-IDEX-04-LUE); CPER (SusChemProc); Deutsche Forschungsgemeinschaft (grant No. DFG INST 190/165-1 FUGG to Mirco Imlau); Deutscher Akademischer Austauschdienst (award No. 57390412 to Mirco Imlau).

References

Akl, J., Billot, C., Lacroix, P. G., Sasaki, I., Mallet-Ladeira, S., Malfant, I., Arcos-Ramos, R., Romero, M. & Farfán, N. (2013). *New J. Chem.* **37**, 3518–3527.
 Asselberghs, I., Clays, K., Persoons, A., Ward, M. D. & McCleverty, J. (2004). *J. Mater. Chem.* **14**, 2831–2839.
 Athmani, H., Kijatkin, C., Benali-Cherif, R., Pillet, S., Schaniel, D., Imlau, M., Benali-Cherif, N. & Bendeif, E.-E. (2019). *Acta Cryst.* **A75**, 107–114.

Bourhis, L. J., Dolomanov, O. V., Gildea, R. J., Howard, J. A. K. & Puschmann, H. (2015). *Acta Cryst.* **A71**, 59–75.
 Chemla, D. S. (1980). *Rep. Prog. Phys.* **43**, 1191–1262.
 Clays, K. & Persoons, A. (1991). *Phys. Rev. Lett.* **66**, 2980–2983.
 Coe, B. J., Houbrechts, S., Asselberghs, I. & Persoons, A. (1999). *Angew. Chem. Int. Ed.* **38**, 366–369.
 Coppens, P., Novozhilova, I. & Kovalevsky, A. (2002). *Chem. Rev.* **102**, 861–884.
 Cormary, B., Malfant, I., Buron-Le Cointe, M., Toupet, L., Delley, B., Schaniel, D., Mockus, N., Woike, T., Fejfarová, K., Petříček, V. & Dusek, M. (2009). *Acta Cryst.* **B65**, 612–623.
 Dolomanov, O. V., Bourhis, L. J., Gildea, R. J., Howard, J. A. K. & Puschmann, H. (2009). *J. Appl. Cryst.* **42**, 339–341.
 Fomitchev, D. V. & Coppens, P. (1996). *Inorg. Chem.* **35**, 7021–7026.
 Groom, C. R., Bruno, I. J., Lightfoot, M. P. & Ward, S. C. (2016). *Acta Cryst.* **B72**, 171–179.
 Hirshfeld, F. L. (1977). *Theor. Chim. Acta*, **44**, 129–138.
 Hsieh, C.-L., Grange, R., Pu, Y. & Psaltis, D. (2009). *Opt. Express*, **17**, 2880–2891.
 Kijatkin, C., Eggert, J., Bock, S., Berben, D., Oláh, L., Szaller, Z., Kis, Z. & Imlau, M. (2017). *Photonics*, **4**, 11.
 Kim, E., Steinbrück, A., Buscaglia, M. T., Buscaglia, V., Pertsch, T. & Grange, R. (2013). *ACS Nano*, **7**, 5343–5349.
 Knabe, B., Buse, K., Assenmacher, W. & Mader, W. (2012). *Phys. Rev. B Condens. Matter Mater. Phys.* **86**, 195428.
 Kostin, G. A., Borodin, A. O., Mikhailov, A. A., Kuratieva, N. V., Kolesov, B. A., Pishchur, D. P., Woike, T. & Schaniel, D. (2015). *Eur. J. Inorg. Chem.* **2015**, 4905–4913.
 Kostin, G. A., Mikhailov, A. A., Kuratieva, N. V., Pishchur, D. P., Zharkov, D. O. & Grin, I. R. (2017). *New J. Chem.* **41**, 7758–7765.
 Kostin, G. A., Mikhailov, A. A., Kuratieva, N. V., Pishchur, D. P. & Makhinya, A. N. (2018). *New J. Chem.* **42**, 18928–18934.
 Le Dantec, R., Mugnier, Y., Djanta, G., Bonacina, L., Extermann, J., Badie, L., Joulaud, C., Germann, M., Rytz, D., Wolf, J. P. & Galez, C. (2011). *J. Phys. Chem. C*, **115**, 15140–15146.
 Mikhailov, A. A., Wenger, E., Kostin, G. A. & Schaniel, D. (2019). *Chem. Eur. J.* **25**, 7569–7574.
 Morioka, Y., Ishikawa, A., Tomizawa, H. & Miki, E. (2000). *J. Chem. Soc. Dalton Trans.* pp. 781–786.
 Ookubo, K., Morioka, Y., Tomizawa, H. & Miki, E. (1996). *J. Mol. Struct.* **379**, 241–247.
 Powell, C. E., Cifuentes, M. P., Morrall, J. P., Stranger, R., Humphrey, M. G., Samoc, M., Luther-Davies, B. & Heath, G. A. (2003). *J. Am. Chem. Soc.* **125**, 602–610.
 Roke, S. & Gonella, G. (2012). *Annu. Rev. Phys. Chem.* **63**, 353–378.
 Sakaguchi, H., Nakamura, H., Nagamura, T., Ogawa, T. & Matsuo, T. (1989). *Chem. Lett.* **18**, 1715–1718.
 Schaniel, D., Bendeif, E.-E., Woike, T., Böttcher, H.-C. & Pillet, S. (2018). *CrystEngComm*, **20**, 7100–7108.
 Schaniel, D., Cormary, B., Malfant, I., Valade, L., Woike, T., Delley, B., Krämer, K. W. & Güdel, H. U. (2007). *Phys. Chem. Chem. Phys.* **9**, 3717–3724.
 Schaniel, D., Imlau, M., Weisemoeller, T., Woike, T., Krämer, K. W. & Güdel, H.-U. (2007). *Adv. Mater.* **19**, 723–726.
 Schaniel, D., Woike, T., Delley, B., Boskovic, C., Biner, D., Krämer, K. W. & Güdel, H. U. (2005). *Phys. Chem. Chem. Phys.* **7**, 1164–1170.
 Sinitsyn, M. N., Svetlov, A. A., Kanishcheva, A. S., Mikhailov, Y. N., Sadikov, G. G. & Kokunov, Y. V. B. Y. A. (1989). *Zh. Neorg. Khim.* **34**, 2795–2802.
 Spackman, M. A. & Jayatilaka, D. (2009). *CrystEngComm*, **11**, 19–32.
 Staedler, D., Magouroux, T., Hadji, R., Joulaud, C., Extermann, J., Schwung, S., Passemard, S., Kasparian, C., Clarke, G., Germann, M., Le Dantec, R., Mugnier, Y., Rytz, D., Ciepiewski, D., Galez, C., Gerber-Lemaire, S., Juillerat-Jeanneret, L., Bonacina, L. & Wolf, J.-P. (2012). *ACS Nano*, **6**, 2542–2549.

- Su, J., Zhang, J., Tian, X., Zhao, M., Song, T., Yu, J., Cui, Y., Qian, G., Zhong, H., Luo, L., Zhang, Y., Wang, C., Li, S., Yang, J., Zhou, H., Wu, J. & Tian, Y. (2017). *J. Mater. Chem. B*, **5**, 5458–5463.
- Turner, M. J., McKinnon, J. J., Wolff, S. K., Grimwood, D. J., Spackman, P. R., Jayatilaka, D. & Spackman, M. A. (2017). *Crystal Explorer17*. University of Western Australia, Australia. <http://hirshfeldsurface.net>.
- Urban, B. E., Neogi, P., Senthilkumar, K., Rajpurohit, S. K., Jagadeeshwaran, P., Kim, S., Fujita, Y. & Neogi, A. (2012). *IEEE J. Sel. Top. Quantum Electron.* **18**, 1451–1456.
- Weidemann, M., Sievertsen, S. & Homborg, H. (1998). *Z. Anorg. Allg. Chem.* **624**, 909–918.
- Yamaletdinov, R. D. & Zilberberg, I. L. (2017). *Eur. J. Inorg. Chem.* **2017**, 2951–2954.